Third International Symposium on Marine Propulsors
smp'13, Launceston, Australia, May 2013

Detached Eddy Simulation of the flow behind an isolated propeller

Roberto Muscari[1], **Andrea Di Mascio**[2]

[1]Istituto Nazionale per Studi ed Esperienze di Architettura Navale (INSEAN), Roma, Italy
[2]Istituto per le Applicazione del Calcolo "Mauro Picone" (IAC), Roma, Italy

ABSTRACT

The turbulent flow behind a rotating marine propeller is analysed by integration of the Reynolds-Averaged Navier–Stokes Equations with both the Spalart & Allmaras (1994) eddy viscosity model and by a Detached Eddy Simulation approach (Spalart et al 1997) in order to assess advantages and limits of the two different turbulence models. As far as global quantities (like thrust and torque) are concerned, it is shown that the two methods perform equally well. On the contrary, local flow features (like the evolution of the wake or the onset of tip vortices instability) are capured by DES, whereas the eddy viscosity modelling proves to be overly dissipative.

Keywords

Marine propeller, RANSE, Detached Eddy Simulation, vortex instability

Notations and abbreviations

DES	Detached Eddy Simulation
PSD	Power Spectral Density
U_∞	Undisturbed inflow velocity
n	Revolutions per second
D	Diameter of the propeller
J	Advance coefficient
Rn	Reynolds number
L_{ref}	Reference length $\equiv$ Radius of the propeller
U_{ref}	Reference velocity
ρ_{ref}	Density of the fluid
ν	Kinematic viscosity of the fluid
T	Non–dimensional period of revolution
dt	Non–dimensional time–step
u_i	Absolute velocity component in the propeller frame of reference
ω_i	Non–dimensional angular velocity
p	Non–dimensional hydrodynamic pressure
$\mathbf{S}$	Symmetric component of $\nabla\mathbf{u}$
$\mathbf{\Omega}$	Antisymmetric component of $\nabla\mathbf{u}$
λ_2	Second largest invariant of $\mathbf{S^2} + \mathbf{\Omega^2}$
K	Kinetic energy
κ	Wave number

1 INTRODUCTION

The study of the flow past a marine propeller has high relevance under several points of view. Traditionally, the most important information that is required to a numerical simulation is an accurate prediction of the loads acting on the propeller. In this respect, an inviscid approach like a Boundary Elements Method can already provide satisfactorily results, at least near design conditions, with a relatively low computational effort. However, the ever increasing computing power make possible to investigate finer details of the flow and, moreover, in complex configurations. For example, the authors already considered in (Muscari & Di Mascio 2011, Muscari et al 2011, but other notable examples can also be found in Carrica et al 2010 and Carrica et al 2008) the case of a mounted propeller operating in the wake of a fully appended hull. In that study, for which the RANS method was used, it was possible to extract several valuable information like the strong variation of the loading on each blade depending on the local incoming flow, the evolution of the tip vortices and their interaction with the rudder or the pressure fluctuations on the vault of the stern caused by the propeller rotation.

However, the performances of a RANS in other contexts are not clear. For example, in this paper we consider the vortex system in the wake of an isolated propeller in a uniform flow. This kind of flow has been the subject of an accurate experimental work in Felli et al (2011). Through flow measurements and visualizations, those authors studied the mechanisms that trigger the instability of the wake by using a set of marine propellers with the same hub and blade profiles, but different number of blades (2, 3 and 4) and blade loading. They highlighted the dependence of the vortex pairing and grouping on the mutual vortex distance and gave an overall description of the way the tip vortices interact with each other and with the hub vortex, when varying the operating conditions. Moreover, they showed the way in which the frequency content of the signal is connected to vortex merging and, more in general, to flow instabilities. Aim of the present paper is to investigate to which extent these features can be reproduced by

different types of numerical simulation, specifically RANS and DES. The interest for this analysis is triggered by the possibility to perform noise predictions based, for instance, on the Ffocws-William Hawking formulation (see Ianniello 2007) where the hydrodynamic data are to be used as input for the noise computations. In this context, it is evident that the successfully reproduction of the vortex dynamics and of the related spectra is fundamental for a correct noise analysis.

The paper is arranged as follows: in the next section an overview of the mathematical and numerical models is given, then the test case is described in details and results are shown for two significant advance coefficients, i.e. $J = 0.71, 0, 45$.

2 MATHEMATICAL AND NUMERICAL MODELS

2.1 Mathematical models

The numerical simulation of the flow field is performed by the integration of the Reynolds Averaged Navier–Stokes equations written in non-dimensional form in the frame of reference fixed to the propeller, in terms of absolute velocity components:

$$\begin{cases} \dfrac{\partial u_i}{\partial x_i} = 0 \\ \dfrac{\partial u_i}{\partial t} + \dfrac{\partial}{\partial x_j}\left[\left(u_j - \epsilon_{jlm}\omega_l r_m\right) u_i\right] + \qquad i = 1,2,3 \\ \qquad +\epsilon_{ijk}\omega_j u_k + \dfrac{\partial p}{\partial x_i} - \dfrac{\partial \tau_{ij}}{\partial x_j} = 0 \end{cases} \tag{1}$$

where u_i are the absolute velocity component in the relative system, ω_i is the (constant) angular velocity, $r_i = x_i - x_i^0$ is the position of point x_i with respect to x_i^0, p is the pressure, $\tau_{ij} = \nu_T(\partial u_i/\partial x_j + \partial u_j/\partial x_i)$ the stress tensor, $\nu_T = 1/\mathrm{Rn} + \nu_t$, ν_t being the turbulent viscosity calculated by means of a proper turbulence model and Rn the Reynolds number (later defined).

Proper boundary conditions are enforced at the physical boundaries of the numerical domain. In particular, on the solid walls the velocity of the fluid is set equal to the local velocity of the body; at the inflow, the velocity is set to the undisturbed flow value, whereas at the outflow the velocity is extrapolated from inner points.

In all the simulations shown in the paper, the one–equation model by Spalart & Allmaras (1994) was used for RANSE simulations, whereas the DES approach (Spalart 2009) was applied for the direct simulation of the larger turbulent structures in the wake.

2.2 Numerical models

The numerical algorithm is based on a finite volume technique with pressure and velocity co–located at cell centers. For the viscous terms a standard second order centered scheme is adopted, whereas for the inviscid part the code has a library of different discretization schemes: a second order ENO (Essentially Non Oscillatory) scheme, a third order upwind scheme (Van Leer 1979), a third order WENO scheme (Jiang & Shu 1996) and a fourth order centered scheme (Di Mascio et al 2009). The ENO and WENO algorithms are able to handle flows with strong gradients and even discontinuities with remarkable robustness. Nevertheless, they often introduce too much numerical diffusion that can overshadow the physical viscosity, and the number of points required to capture the generation and evolution of some flow details can became prohibitive. In these cases, the use of a higher order scheme provides the most convenient solution, and, for this reason, all the numerical results shown in this work were obtained with the third order upwind scheme for steady RANSE simulation and the centered fourth–order scheme for the DES simulations. It should be stressed that the formal spatial accuracy of this method is second–order (owing to the treatment of the viscous terms); nevertheless, the use of a less dissipative scheme for the convective terms allows to follow the formation and convection of strong gradients (in particular, vortex cores) for a considerably longer distance than with the use of a second order–scheme (see, for example (Muscari et al 2011)).

The physical time–derivatives in the governing equations are approximated by a second–order accurate, three–point backward finite difference formula (Di Mascio et al 2009); the discrete equation being fully implicit, no stability restriction exists on the time step, that can be chosen on the basis of accuracy alone.

In order to obtain a divergence free velocity field at every physical–time step, a dual- or pseudo–time derivative is introduced in the discrete system of equations (Merkle & Athavale 1987). The convergence ratio for the inner iteration is accelerated by means of local time stepping, an implicit Euler scheme with approximate factorization (Beam & Warming 1978) and a multi–grid technique (Favini et al 1996).

3 TEST CASE DESCRIPTION

The test case chosen for our investigation is the same as that described in Felli et al (2011), where the evolution of the tip and hub vortices in the wake of a marine propeller were experimentally studied in a water tunnel. For our purposes, that investigation is particularly convenient, as it deals with a relatively simple geometry (a propeller in open water, hence, with no free–surface to be taken into account), with a wealth of flow visualization details and a variety of different propeller loadings. In fact, since in the numerical simulation the extension of the resolved field past the propeller had necessarily to be limited, we focused our computations on low advance coefficients (high loading) for a four blade propeller, in order to limit our simulation to those cases where the vortices break–down "close" to the propeller.

The propeller geometry is the INSEAN E779A model, i.e. a four blade, fixed–pitch, right–handed propeller characterized by a nominally constant pitch distribution and a very low skew. Views of the propeller are shown in figure 1 whereas the main geometrical features are reported in Table 1. More information on the propeller, can be found in Salvatore et al (2006).

4 NUMERICAL SIMULATION SET–UP

In the numerical simulations, the rotational speed of the propeller has been kept fixed to a value of $n = 25\,rps$ and the different advance coefficients $J = U_\infty / n\,D$ are obtained by changing the inflow velocity U_∞. Unless otherwise specified, all quantities have been cast in non–dimensional form by using as reference values the radius of the propeller ($L_{ref} = 0.1135\,m$), the velocity of the tips of the blades ($U_{ref} = n\,\pi\,D \simeq 17.85\,m/s$) and the density of fluid ($\rho_{ref} = 1000\,kg/m^3$). Therefore, the non–dimensional period of revolution is $T = 2\,\pi$. The Reynolds number is the same of the physical experiment, i.e. $\mathrm{Rn} = U_{ref}\,L_{ref}/\nu = 1.78 \cdot 10^6$.

In order to give an estimation of the numerical uncertainty, two grid levels were used, the coarser being obtained by removing every other point from the finer. The computation being performed in the rotating non–inertial frame of reference, a steady solution was obtained for the RANSE simulation; for the DES simulation, the solution was computed by including the physical time derivatives, and the chosen time step was always corresponding to a rotation of one degree for the propeller ($dt = 2\,\pi/360 \simeq 0.01745$), in the case of the finer grid. As already stated in the section devoted to the numerical model, no stability restriction exists on the time step, and this particular value for dt was chosen to get a sufficient resolution in the analysis of the time signals.

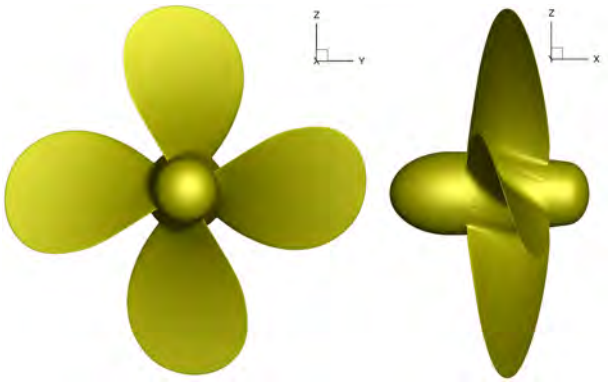

Figure 1: Front and side views of the propeller model.

In order to give an idea of the cell clustering, in figure 2 a slice of the volume mesh in the plane $y = 0$ is reported. In particular, the resolved part (finer grid) of the computational domain extends up to 4.4 radii downstream of the reference plane ($x = 0$) of the propeller, and this is the

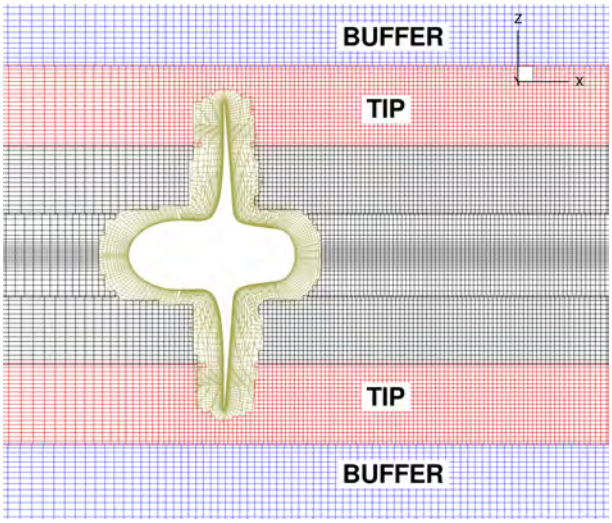

Figure 2: Details of the volume mesh. Section $y = 0$.

region within which we can expect to be able to properly capture the main flow features (tip and hub vortices). The extension of the resolved zone was dictated by a necessary trade–off between the need to follow the wake as farther as possible and to limit the total number of computational cells.

The boundary layer is resolved by about 32 cells, the center of the first cell being set at a distance $y^+ < 1$, in wall units, from wall. Apart from the blocks fitted around the geometry, most of the cells are placed in the toroidal block that is used to track the tip vortices; another external toroidal block is used as a buffer between the finer mesh near the propeller and the outer, coarser, background mesh. The different blocks sum up to a total of 11M cells.

Regarding the initial conditions, the steady RANSE simulations started from a uniform flow condition (with U_∞ prescribed by the advance coefficient under analysis), whereas the unsteady DES simulations started from the corresponding (i.e. with the same advance coefficient) RANSE computation.

INSEAN E779A model	
Diameter	$D = 0.227$ m
Number of blades	$Z = 4$
Pitch ratio	$P/D = 1.1$
Expanded area ratio	0.689
Hub ratio	0.200

Table 1: Propeller parameters.

5 RESULTS

5.1 Thrust and torque

For a first check of the performances of the different approaches, we considered the open water characteristics of the model. In figure 3 several numerical results for differ-

ent values of the advance coefficient are superposed to the experimental curves (Salvatore et al 2006).

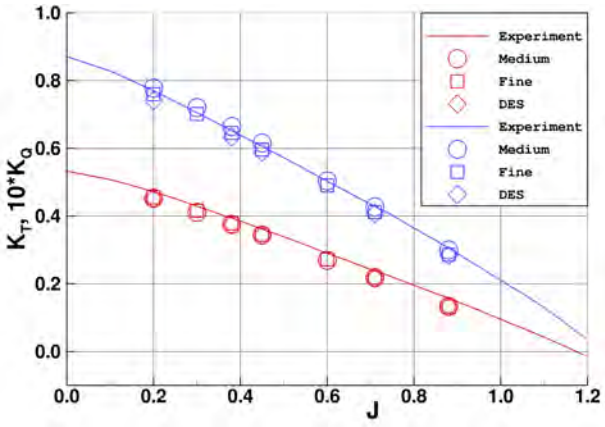

Figure 3: Measured and predicted open water characteristics of the E779A propeller.

The thrust predicted by the RANSE (on both coarse and fine meshes) and DES (on the fine mesh, only) is essentially identical for all values of the advance coefficient. The difference between computed and measured values is almost constant in the whole simulation range, although it is smaller in percent of the computed values at low values of J (being about 4% of the experimental value) and grows with J up to a difference of about 15% for $J = 0.88$, where both the computed and the measured values of the force become very small. In addition, it has to be noted the lack of uncertainty estimation of the experimental data.

The torque shows a greater sensitivity to mesh refinement, its value being strongly dependent on a correct estimation of the viscous forces in the boundary layer. In particular, it can be noticed a shift of the whole curve towards lower values as the grid gets finer. In any case, the experimental data fall within the range of numerical uncertainty. The use of a DES model, in place of the RANSE simulation, produces some effects only for lower values of J, the differences being irrelevant for higher values.

The agreement among the computed forces for the different turbulence modeling (DES and RANSE) is not surprising, since in both cases the boundary layers have been modelled using Spalart & Allmaras model and therefore the observed small differences are to be ascribed only to the different vorticity field in the wake of the propeller.

It can be concluded that, from the point of view of global quantities estimation, there seems be no point in using a more accurate turbulence model or even a highly refined mesh.

5.2 Flow field in the wake

The following analysis of the flow field has been carried out for two values of the advance coefficient, namely $J = 0.71, 0.45$. These values have been considered in order to try to reproduce some of the findings of Felli et al (2011) and to validate the numerical simulations. In particular, for the four–blade configuration at $J = 0.71$, the detailed frequency analysis performed in the experimental work illustrates the process of energy transfer from the blade harmonic to the shaft harmonic along the longitudinal direction, owing to vortex grouping. Unfortunately this process takes place after a long distance downstream of the propeller (in the original reference it develops at a distance $x = 12.65\,R$), whereas the refined computational mesh terminates only at $x = 4.4\,R$. In order to be able to capture at least the first stages of the vortex coupling phenomenon described in the experimental work, we repeated the simulation for $J = 0.45$ (which is the lowest value of the advance coefficient reported in Felli et al (2011)).

Simulations for $J = 0.38, 0.2$ will be perfomed in the following of the research.

5.2.1 J=0.71

A general overview of the vorticity field in the wake of the propeller is given in figure 4. The surface shown in the figure corresponds to the non–dimensional value $\lambda_2 = -2$ of the second largest invariant of $\mathbf{S^2} + \mathbf{\Omega^2}$ ($\mathbf{S}$ and $\mathbf{\Omega}$ being the symmetric and antisymmetric components of $\nabla\mathbf{u}$, respectively (Jeong & Hussain 1995)) and it is coloured by pressure levels. After a slight, initial reduction of the radial position of the vortex cores, caused by the acceleration of the flow behind the propeller, the helices formed by the tip vortices remain located on a cylinder of almost constant radius up to the end of the refinement blocks. This simulation reproduce the experimental findings visualized in Felli et al (2011) for $J = 0.65$ and $J = 0.75$, where the destabilization process take place beyond the limit of finely discretized domain in the numerical simulation.

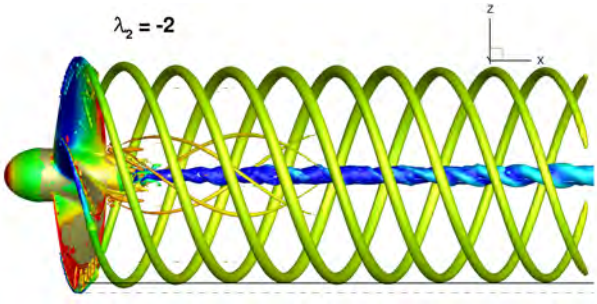

Figure 4: $J = 0.71$. Vorticity field visualization for DES.

In order to have at least a qualitative idea of the level of resolution obtained with the grid employed in the simulations, we computed the amount of resolved kinetic energy (that is, $\mathrm{TKE}_{res} = \frac{1}{2}\left(u'^2 + v'^2 + w'^2\right)$) in the wake of the propeller and compared it with a quantity that can give an estimation of the modeled part (as well known, in a Boussinesq's approximation of turbulent stresses, the modelled kinetic energy is absorbed in the pressure terms and cannot be discerned from it)

$$\mathrm{TKE}_{mod} = \frac{1}{2}\,\nu_{turb}\left(\left|\frac{\partial u}{\partial x}\right| + \left|\frac{\partial v}{\partial y}\right| + \left|\frac{\partial w}{\partial z}\right|\right). \qquad (2)$$

This two quantities are compared in figure 5, where it can be seen that the modelled part of the TKE is reasonably small when compared to TKE_{res}. This shows that cell size is small enough to resolve the largest velocity scale fluctuations. Moreover, the low maximum value of TKE_{res} corresponds to a very stable wake.

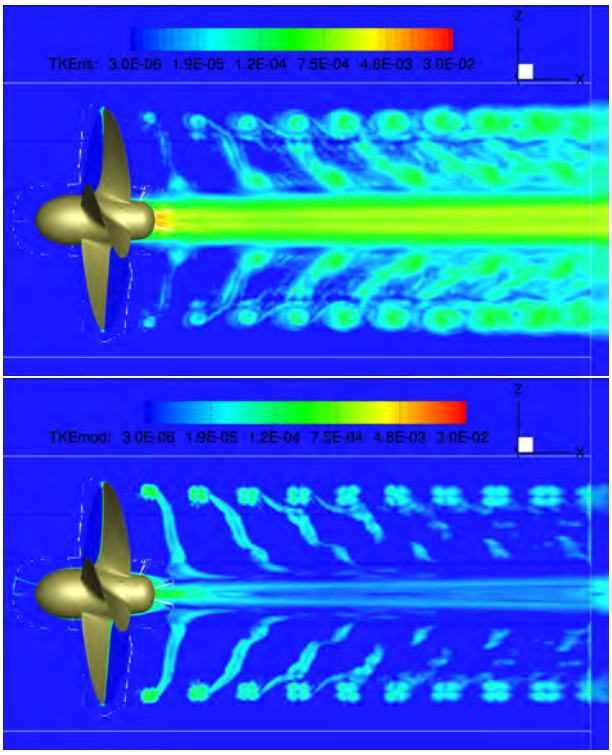

Figure 5: Turbulent kinetic energy for $J = 0.71$; resolved (up), modeled (according to equation 2, down).

A partial validation of the numerical results can be done by comparing the computed power spectral density of the kinetic energy with the analogous experimental data reported in Felli et al (2011). Numerical data were collected as in the experiments, i.e. we set a series of "probes" in the inertial frame of reference at a distance $r = 0.9R$ from the axis of the propeller and at several stations downstream (figure 6) and the time histories of the kinetic energy were recorded; then, we have computed the power spectral density (PSD) of the kinetic energy $K = 0.5\left(u^2 + v^2 + w^2\right)$. The result for three probes are shown in figure 12, where the wave numbers have been scaled so that the blade frequency is $\kappa = 1$. In particular, the first two probes have been selected in order to make a direct comparison with experiments (see figure 40 in Felli et al (2011)) and the third one is placed at the farther distance allowed by the numerical grid, being near the boundary of the inner fine computational mesh. Several observations can be done from the reported graphs.

For $X = 0.35\ R$, very close to the blade tips, the spectrum exhibits sharp peaks at the blade frequency and all its multiples, indicating a low level of noise superimposed to the tonal components. Although the experimental spectra in Felli et al (2011) are truncated at a frequency only slightly higher than twice the blade frequency, at this probe position they also show well defined peaks for $\kappa = 1$ and $\kappa = 2$.

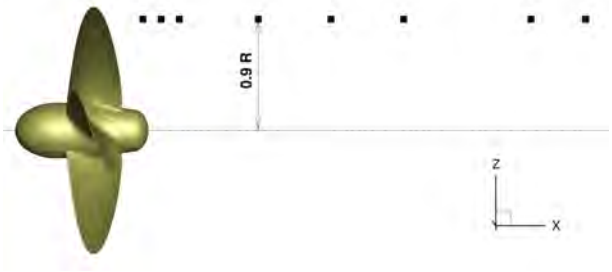

Figure 6: Probes positions relative to the PSD in figure 12.

If we inspect the data at $X = 3.55\ R$, the energy transfer thoroughly described in Felli et al (2011) is beginning to appear also in the numerical data; in particular, a smaller peak for $\kappa = 0.5$ is evident in the spectrum indicating an incipient pairing between the tip vortices. The main difference between CFD and measurements is the presence (in the experiments) of a strong peak for $\kappa = 1.5$ which is visible in the numerical spectrum although not as strong as in the experiments. The last station that could be numerically considered, $X = 4.0\ R$, has no counterpart in Felli et al (2011), but it is very interesting as it shows both a more pronounced peak at $\kappa = 1.5$ and a first appearance of a peak at the shaft frequency ($\kappa = 0.25$) which is, according to the experiment, the only contribution to the spectrum when the process of energy transfer completes. In figure 12 is also shown, through the red line $\kappa^{-0.9}$, that the power-law decay found in the experiments is very well captured.
As to the question regarding the need of a DES simulation with respect to a much faster RANSE approach, a comparison between the predictions of the flow fields, obtained by the two different turbulence models is given in figure 7; here, the results from the steady RANSE computation are compared to the field obtained by averaging 3600 instantaneous fields (i.e. 10 revolutions) from the unsteady DES. In particular, the figure shows a longitudinal cut of the axial velocity field. The main flow characteristics are the same for the two approaches, with a well defined zone of accelerated flow, in which the traces of the tip vortices and the wakes of the blades, together with a central zone past the hub of slower fluid, are evident. However, all these features are very smoothed in the RANSE simulation, and some are completely missing (like the very low velocity zone in the core of the hub vortex). Moreover, when comparing the resolved vortical structures (figure 8 for RANS and figure 4 for DES), it is clear that the RANSE model yields tip vor-

tices than vanish after a length of about a propeller diameter. These differences are caused by a too high level of viscosity introduced by the RANSE turbulence model.

5.2.2 J=0.45

This value of the advance coefficient is the lowest one for which visualizations are reported in Felli et al (2011), and has been analysed in order to check whether the numerical simulation was able to capture the vortex pairing phenomenon, which for this J begins (by a mere observations of the photographs) around $X = 0.3R$.
In figures 9-10, similarly to the case $J = 0.71$, the comparison between RANSE and DES simulation is reported. In particular, figure 10 should represent the analogous of the upper–right frame of figure 8 in Felli et al (2011), where the pairing of tip vortices and the incipient instability of the hub vortex are visualized.

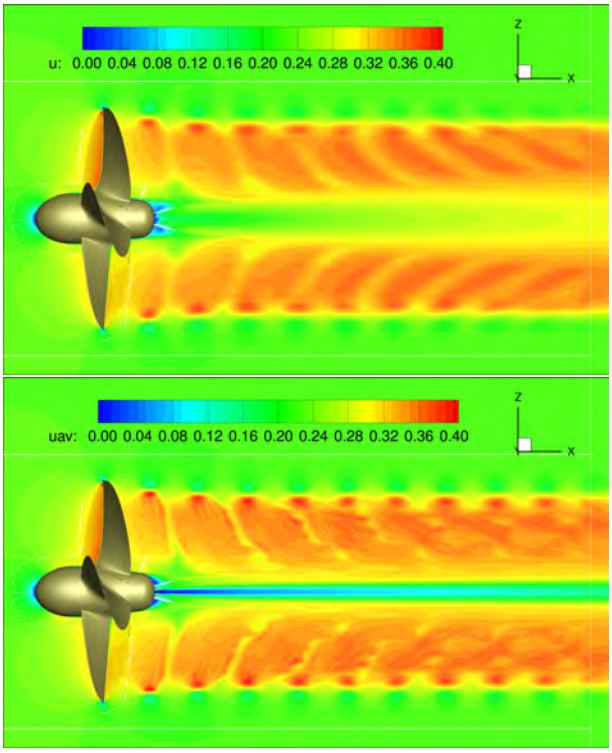

Figure 7: $J = 0.71$. Section x-z of the axial velocity field. RANSE (up) and running averages from DES (down).

The higher thrust obtained for this value of the advance coefficient J (and therefore the higher blade loading) manifests both in the faster deformation of the wakes that, in the inner part of the slipstream, become rapidly aligned to the flow, and in the stronger tip vortices (it should be noted that the velocity contour levels are the same as in figure 7). In comparison with the DES, the RANSE approach seems to introduce even more viscosity than in the case $J = 0.71$, as in the last part of the resolved region of the wake the velocity gradients, still very strong in the DES, are completely blurred. It is also significant that, despite the fact

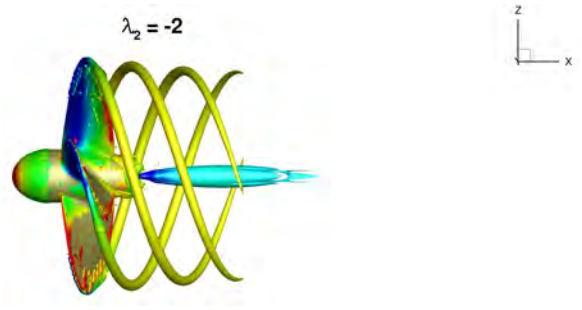

Figure 8: $J = 0.71$. Vorticity field visualization for RANSE.

that the tip vortices are stronger than in the previous case, they can be tracked for a shorter distance (see figure 8 for comparison) before being dissipated. This trend evidently means that the growth of turbulent viscosity in the Spalart & Allmaras (1994) model triggered by the velocity gradients is, for this kind of computation, definitely too high. On the other hand, the DES permits to track the vortices up to the end of the resolved mesh, and it effectively shows both the onset of the vortices instability and the start of the pairing process described in the experiments. A visual comparison of the bottom part of figure 10 with the corresponding photograph in Felli et al (2011) shows a striking similarity, with the features of the configuration marked by red ellipses identical in both data sets. Actually, there is a difference in the starting point of the transition to instability, the numerical one being retarded with respect to the experimental one.

With respect to the case $J = 0.71$, the intensity of the resolved TKE (figure 11) has grown, in particular towards the end of the resolved mesh where the instability process begins, whereas the modeled TKE is limited to lower levels. In the plot of the resolved TKE, it is interesting to note the start of the pairing process between the two couples of tip vortices that is revealed with extreme clarity.

This pairing process can also be seen from the analysis of the power spectral density of the kinetic energy. At $x = 0.35\,R$ (figure 13) well defined peaks at the blade frequency and its multiples can be observed, as expected because of the small distance from the propeller plane. However, at a distance $x = 2.5\,R$ most of the peaks have vanished and the whole curve has shifted to higher values, suggesting a higher noise content. The only peaks that still characterize the spectrum are for $\kappa = 1$ plus, though with a smaller magnitude, $\kappa = 0.5$ and $\kappa = 1.5$, these latter indicating the process of incipient vortex coupling already observed previously. At $x = 3.55\,R$ the whole spectrum has further increased in magnitude and, apart from a small peak corresponding to the blade frequency, no other harmonic component seems to characterize it. As for the case $J = 0.71$, we found a power–law decay $\kappa^{-0.9}$.

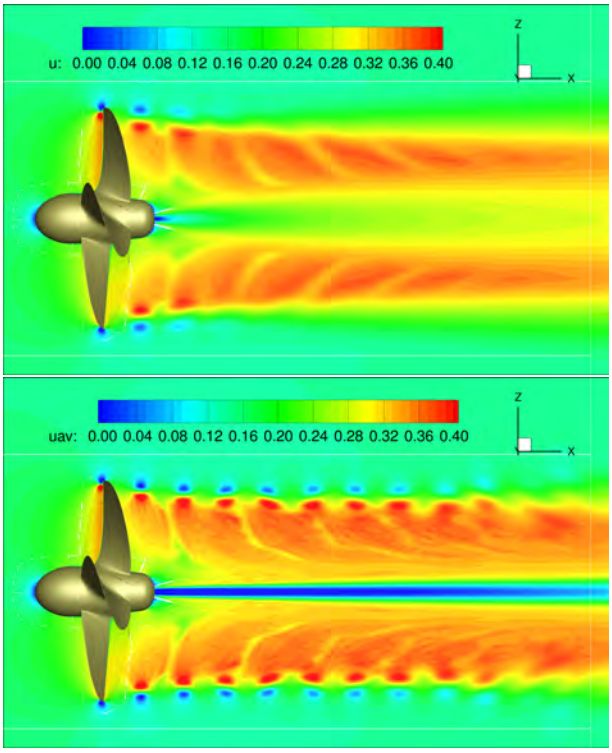

Figure 9: $J = 0.45$. Section x-z of axial velocity. RANSE (up) and running averages from DES (down).

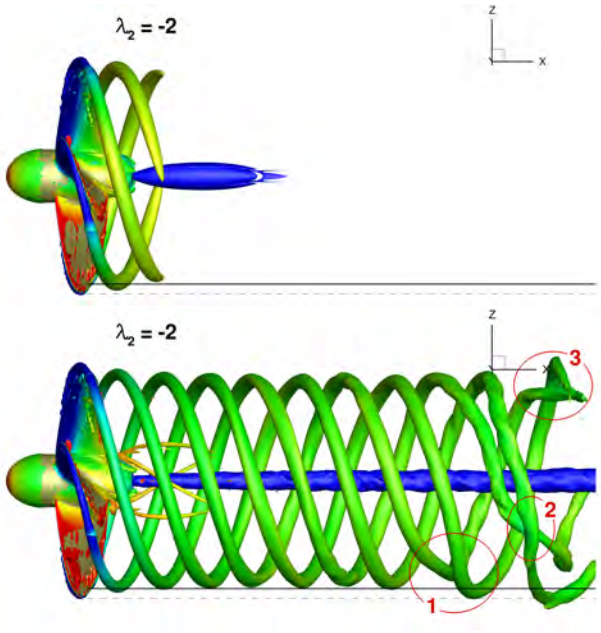

Figure 10: $J = 0.45$. Vorticity field visualization. RANSE (up) and running averages from DES (down).

6 CONCLUSIONS

Two approaches for the simulation of turbulent flows, a RANS method and a DES, have been applied to the study of an isolated marine propeller in uniform flow. The aim of the analysis was to assess the capabilities of these two methods in yielding different levels of information about a fundamental branch of naval engineering.

As a first level, integral quantities like thrust and torque have been considered comparing the experimental open water characteristics with a series of simulations at different values of the advance coefficient. The numerical results are very similar to each other and in good agreement with measurements. In this sense, a RANS is perfectly suitable for predicting the propeller performances and the use of a DES, with the consequent increase of the computing burden, is not justified by a corresponding improvement of the results. Moreover, it has been observed that the number of computational cells must not be exceedingly high, as fine results can also be obtained with a relatively coarse grid.

In order to investigate the wake structure and turbulence dynamics, two loading conditions have been analysed in details, i.e. $J = 0.71$ and $J = 0.45$. The comparison between the Spalart–Allmaras eddy–viscosity model and the DES approach (resting itself on the Spalart–Allmaras model) shows that the RANSE approach dissipates the vorticity field very quickly and, being all other parameters (the computational mesh and integration scheme) identical to the corresponding DES, this over–dissipation has been ascribed to the eddy–viscosity modeling. Furthermore, the growth of turbulent viscosity, strictly connected to the velocity gradients, is such that the stronger the tip vortices (for low values of J), the sooner they are dissipated (and, hence, the shorter distance they can be tracked).

On the contrary, the DES method allows to capture the tip vortices evolution as long as the mesh is reasonably refined with a good qualitative and quantitative agreement with experiments. In particular, the initial stages of the instability pattern, with two consecutive vortex filaments swapping their relative position because of the mutual interaction, can also be reproduced and follow with striking similarity the flow visualizations from water channel experiments. In this respect, the main limit of the computations seems to be the length of the resolved mesh, that is the number of computational volumes. The analysis of the power spectral densities of the signals at different downstream locations has also been performed. Although the resolved field was not sufficiently extended and we could provide information only up to $X = 4.0\ R$, numerical simulations were able to confirm the process of energy transfer, from the blade- to the shaft–frequency components, associated to the vortex pairing observed in the flow visualizations. Moreover, the same power–law decay measured in the experiments was found in the numerical spectra, as a verification of the correct representation of the energy transfer between turbulent scales. A further check on the quality of the DES is given in terms of comparison between the resolved part and (an estimate of) the modeled part of the turbulent kinetic energy: the latter proves to be smaller than the former when a fully turbulent flow is to be expected, confirming that the

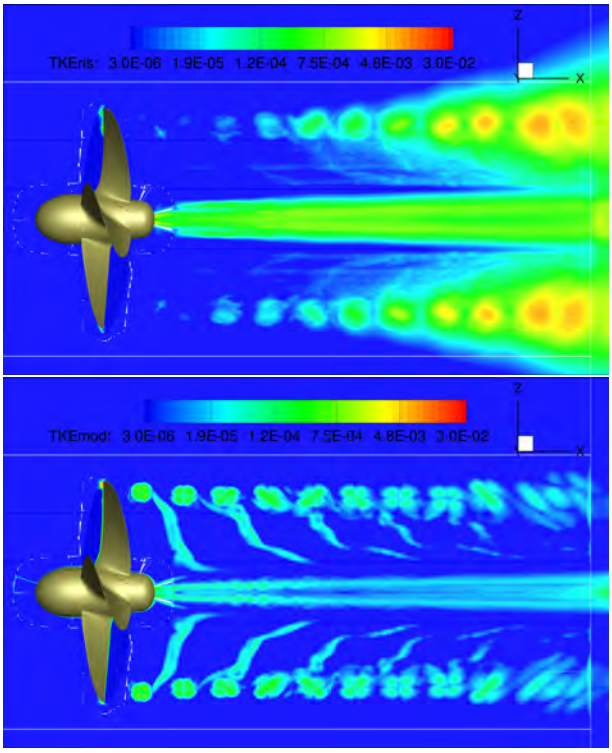

Figure 11: Turbulent kinetic energy for $J = 0.45$; resolved (up), modeled (according to equation 2) (down).

grid resolution was enough to resolve the largest scales of velocity fluctuations.

7 ACKNOWLEDGMENTS

This work was partially supported by the Italian Ministry of Education, University and Research through the research project RITMARE. Numerical computations presented here have been performed on the parallel machines of CASPUR Supercomputing Center (Rome); their support is gratefully acknowledged.

REFERENCES

Beam, R. M. & Warming, R. F. (1978). An Implicit Factored Scheme for the Compressible Navier-Stokes Equations. AIAA Journal, 16, pp. 393–402.

Carrica, P. M., Castro, A. M. & Stern, F. (2010). Self-propulsion computations using a speed controller and a discretized propeller with dynamic overset grids. J. Mar. Sci. Technol., 15(4), pp. 316–330.

Carrica, P. M., Ismail, F., M., H., S., B. & F., S. (2008). Turn and zigzag manoeuvres of a surface combatant using a URANS approach with dynamic overset grids. Proc. SIMMAN 2008 Workshop on Verification and Validation of Ship Manoeuvering Simulation Methods, Copenhagen, Denmark.

Di Mascio, A., Broglia, R. & Muscari, R. (2009). Prediction of hydrodynamic coefficients of ship hulls by high-order Godunov-type methods. J. Mar. Sci. Technol., 14, pp. 19–29.

Favini, B., Broglia, R. & Di Mascio, A. (1996). Multi–grid Acceleration of Second Order ENO Schemes from Low Subsonic to High Supersonic Flows. Int. J. Num. Meth. Fluids, 23, pp. 589–606.

Felli, M., Camussi, R. & Di Felice, F. (2011). Mechanisms of evolution of the propeller wake in the transition and far fields. J. Fluid Mech., 682, pp. 5–53.

Ianniello, S. (2007). New perspectives in the use of the Ffowcs Williams–Hawkings equation for aeroacoustic analysis of rotating blades. J. Fluid Mech., 570, pp. 79–127.

Jeong, J. & Hussain, F. (1995). On the identification of a vortex. J. Fluid Mech., 285, pp. 69–94.

Jiang, G.-S. & Shu, C.-W. (1996). Efficient Implementation of Weighted ENO Schemes. J. Comput. Phys., 126(1), pp. 202–228.

Merkle, C. L. & Athavale, M. (1987). Time–Accurate Unsteady Incompressible Flow Algorithm Based on Artificially Compressibility. AIAA Paper 87–1137.

Muscari, R. & Di Mascio, A. (2011). Numerical simulation of the ow past a rotating propeller behind a hull. Proceedings of the Second International Symposium on Marine Propulsors (SMP'11), Hamburg, Germany.

Muscari, R., Felli, M. & Di Mascio, A. (2011). Analysis of the Flow Past a Fully Appended Hull with Propellers by Computational and Experimental Fluid Dynamics. ASME J. Fluids Eng., 133(6).

Salvatore, F., Pereira, F., Felli, M., Calcagni, D. & Di Felice, F. (2006). Description of the INSEAN E779A propeller experimental dataset. Technical report, INSEAN Tech. Rep. 2006-085.

Spalart, P. R. (2009). Detached-Eddy Simulation. Annu. Rev. Fluid Mech., 41, pp. 181–202.

Spalart, P. R. & Allmaras, S. R. (1994). A one–equation turbulence model for aerodynamic flows. La Recherche Aérospatiale, 1, pp. 5–21.

Spalart, P. R., Jou, W.-H., Strelets, M. & Allmaras, S. R. (1997). Comments on the feasibility of LES for wings, and on a hybrid RANS/LES approach, pages 137–147. Greyden Press, Columbus, OH.

Van Leer, B. (1979). Towards the ultimate conservative difference scheme V. A second–order sequel to Godunov's method. J. Comput. Phys., 32(1), pp. 101–136.

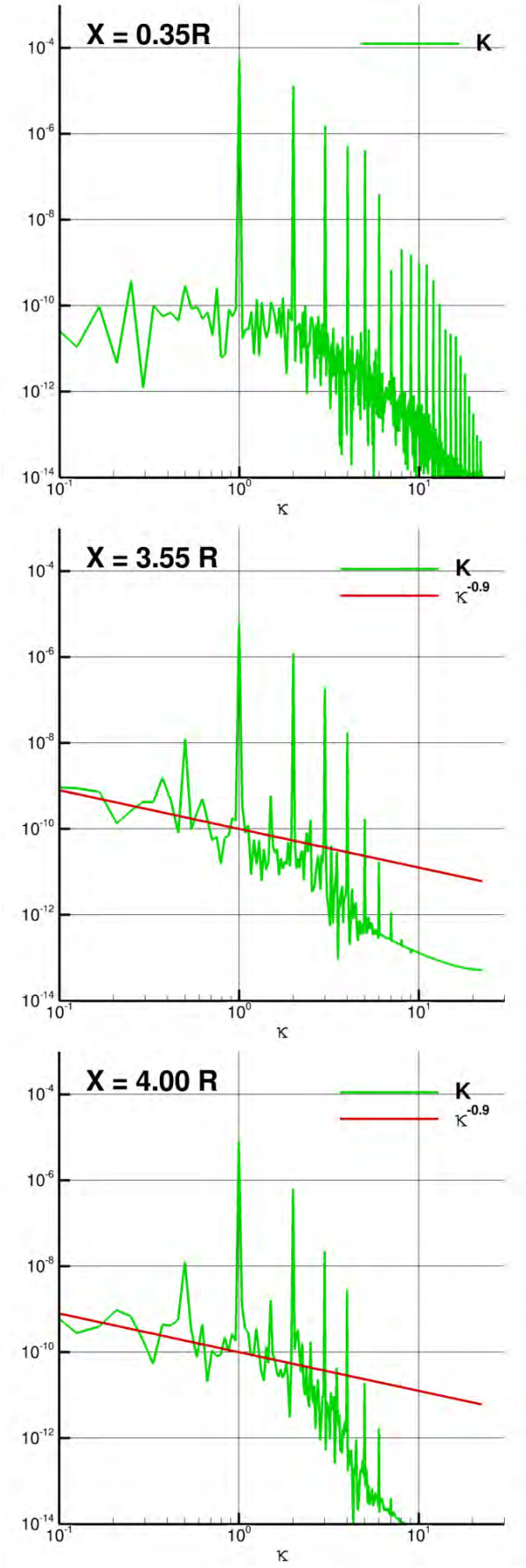

Figure 12: $J = 0.71$ - Numerical PSD of the kinetic energy at different stations downstream the propeller.

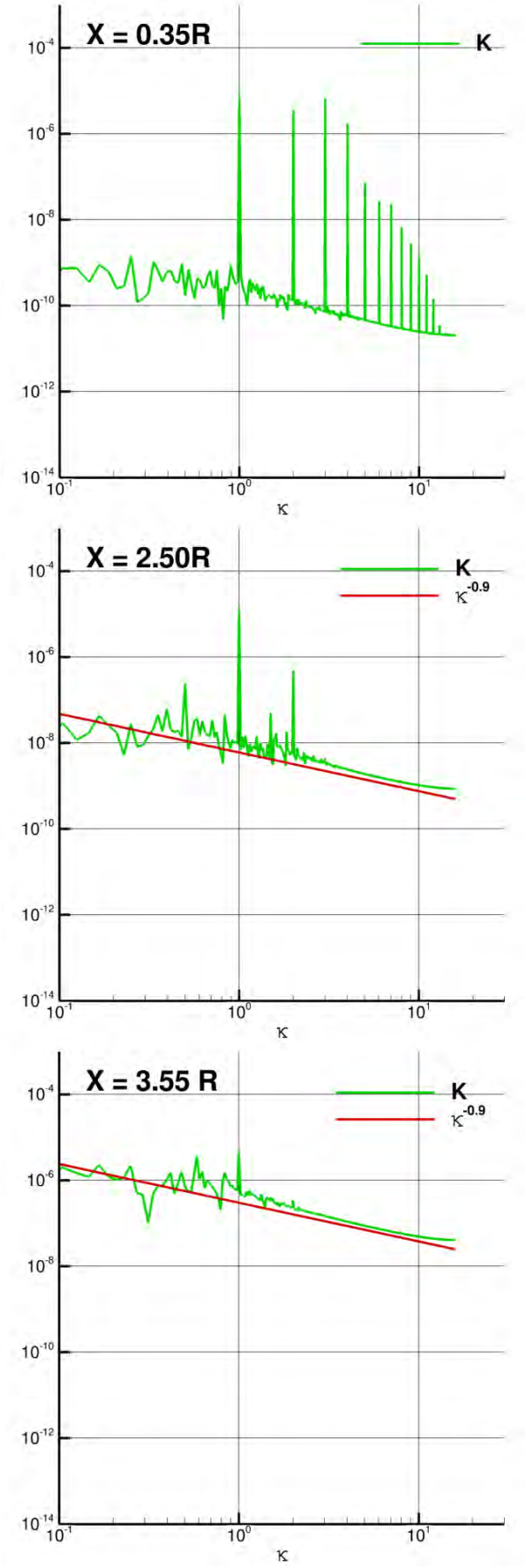

Figure 13: $J = 0.45$ - Numerical PSD of the kinetic energy at different stations downstream the propeller.